

# Chapter 2

## Brief survey of $\text{Na}_x\text{CoO}_2$

### 2-1 Fundamental properties

#### 2-1-1 Structure of $\text{Na}_x\text{CoO}_2$

$\text{Na}_x\text{CoO}_2$  has a crystal structure consisting of Na layers sandwiched between planes of edge shared  $\text{CoO}_6$  octahedra. Fig. 2 - 1 shows the structure of  $\text{CoO}_2$  layer;<sup>[13]</sup> Co atoms are at the center of the octahedra forming a 2D triangular lattice. Oxygen octahedra have a trigonal distortion—a stretch along a body diagonal direction of the embedding cube. The structure of  $\text{Na}_x\text{CoO}_2$  is divided into two parts: two-layer and three-layer systems. Fig. 2 - 2<sup>[14]</sup> illustrates a comparison of the Co positions in the two-layer and three-layer variants. In the two-layer systems the Co planes are the same in all layers. In the three-layer derived systems the triangular Co planes are staggered.

Four different phases have been previously reported in the thermodynamic  $\text{Na}_x\text{CoO}_2$  chemical system by C. Fouassier *et al.* in 1973.<sup>[15]</sup> Three of these four phases are reported to be three-layer structures, delineated as (1) the  $\alpha$  phase ( $O3$  structure) for  $0.9 \leq x \leq 1$ , (2) the  $\alpha'$  phase ( $O1$  structure) for  $x = 0.75$ , and (3) the  $\beta$  phase ( $P1$  structure) for  $0.55 \leq x \leq 0.6$ , while only one thermodynamic phase has a two-layer structure; it is known as the  $\gamma$  phase ( $P2$  structure, including  $H1$ ,  $H2$ , and  $H3$  structures), for  $x \sim 0.7$ . Fig. 2 - 3 displays the structural models for three-layer systems, while Fig. 2 - 4 shows their phase diagram.<sup>[14]</sup> Although different crystal structures are found for the three-layer as opposed to the two-layer structures (as

shown in Table 2 - 1<sup>[13,16-18]</sup>), the basic electronic properties of these materials are similar, supporting the general understanding that the electronic systems, dominated by the in-plane character of the CoO<sub>2</sub> layers, are highly two dimensional in character.<sup>[13]</sup> Therefore, we will focus on the two-layer systems consequently.

Two-layer systems of Na<sub>x</sub>CoO<sub>2</sub> are hexagonal and consist of firm layers of CoO<sub>2</sub> interspersed by Na layers with two inequivalent sites. The basic structures are shown schematically in Fig. 2 - 5,<sup>[7]</sup> while Fig. 2 - 6<sup>[19]</sup> summarizes the composition stability regions and general structural characteristics of the four phases found for Na<sub>x</sub>CoO<sub>2</sub> (The *O1* phase is the orthorhombic insulating phase at  $x = 0.5$ ). Schematic representations of the Na ion positions in the charge reservoir layer are at the top of the figure. It is very interesting to note that for all Na<sub>x</sub>CoO<sub>2</sub> systems including the hydrated one, the  $z$ -axis of the crystal field (in Co-O coordinates) is tilted away from the crystallographic  $c$ -direction by nearly about 60°. In addition, the CoO<sub>6</sub> octahedra are distorted (compressed along the (111) direction in Co-O coordinates) from the ideal configuration, as shown in Fig. 2 - 7.<sup>[20-23]</sup>

For the Na content from  $0.34 < x < 0.74$  (with the exception of  $x = 0.5$ ), they are well described by a structure in which both sodium site are partially occupied and the Na(2) ions are displaced from the ideal centers of the NaO<sub>6</sub> triangular prisms, i.e., in the Na(2)' sites.<sup>[24]</sup> When a particular Na(2)' site (or Na(2) site at higher concentrations) is occupied, while its nearest-neighbor Na(1) sites are excluded from occupancy, as they are too close together to both accommodate Na ions simultaneously. This structure type covers a large fraction of the phase diagram, and is called the *H1* phase. A different structure type is identified for  $0.76 < x < \sim 0.82$ , designated as *H2*, has all the Na(2) ions (when this site is occupied) directly in the center of the ideal Na(2) triangular prism, as well as Na ions on the (partially

occupied) Na(1) site.

The  $H1$  and  $H2$  phases are separated by a narrow two-phase region, and samples of nominal Na stoichiometry  $x \sim 0.75$  show interesting phenomenon that are mixtures of both phases. In the  $H1$  structure, the  $a$ -axis is significantly shorter and the  $c$ -axis is significantly longer than for the  $H2$  structure, which allows these two structures to be readily distinguished from each other in diffraction data, as shown in Fig. 2 - 8,<sup>[25]</sup> suggesting that a sudden change occurs at  $x$  near 0.75, in which structure  $H1$  is the stable phase below  $x \sim 0.75$ , while structure  $H2$  is the stable phase above  $x \sim 0.75$ .

Furthermore, Fig. 2 - 9 shows the (109) Bragg peak of  $x = 0.75$  powder sample over a range of temperatures measured by Q. Huang *et al.* to characterize this structural phase transition in detail.<sup>[25]</sup> At 290 K, there are two diffraction peaks, (109)- $H1$  and (109)- $H2$ , signifying the coexistence of the  $H1$  and  $H2$  structures, respectively. Moreover, with increasing temperature the  $H1$  phase fraction suddenly begins to increase above 320 K and reaches a maximum near 340 K, while the intensity for the  $H2$  peak levels off. Above this temperature the sample is single phase, possessing only the  $H1$  structure. The change in position from Na(2)' to Na(2) sites is abrupt, indicating that at a critical Na layer filling the system suddenly favors on-center Na(2) ion occupancy. The reason for this behavior is not yet understood.

In the  $H1$  and  $H2$  phases, both Na sites are partially occupied, and for general  $x$  the site occupancies are inequivalent and vary systematically with  $x$ .<sup>[19,20,25]</sup> However, there are two cases where the crystal structure is well ordered. One is for Na half filling ( $x = 0.5$ ) with the  $O1$  phase, however, these two sites are occupied in equal proportions, and the material is a charge ordered (antiferromagnetic) insulator at low temperatures.<sup>[26]</sup> In this state a superstructure develops in the Na plane that separates

the  $\text{CoO}_2$  planes and it has been suggested that the insulating state is induced by this superstructure.<sup>[27]</sup> The other case is for  $x = 1$ , designated  $H3$  phase, is found after another two-phase coexistence region ( $H2 + H3$ ). In this compound, all the Na(1) sites are empty and all the Na(2) sites are fully occupied; the Na are all in ideal trigonal prismatic sites that share only edges with the  $\text{CoO}_6$  octahedra.<sup>[19]</sup> The crystal structure of  $H3$  is distinctly different from that of the thermodynamically stable phase  $\text{NaCoO}_2$ , which has all the Na in octahedral coordination with oxygen.<sup>[27]</sup>

## 2-1-2 Superconductivity of $\text{Na}_x\text{CoO}_2$

At lower Na content the recent discovery of superconductivity in hydrated  $\text{Na}_x\text{CoO}_2$  ( $T_c \sim 5$  K) has been of particular interest with regard to the superconducting cuprates.<sup>[2,17]</sup> Taking into account the non-superconducting magnetic phase, the  $x - T$  and  $H - T$  phase diagrams may be depicted as Fig. 2 - 10.<sup>[28]</sup> The superconducting region is separated into two parts of SC1 and SC2 sandwiching the magnetically ordered  $M$  phase, suggesting that the superconductivity is induced by moderately strong magnetic interactions. For the  $\text{Na}_{0.3}\text{CoO}_2 \cdot 1.4\text{H}_2\text{O}$  superconductor, the water forms two additional layers between the Na and  $\text{CoO}_2$ , increasing the  $c$ -axis lattice parameter of the hexagonal  $P6_3/mmc$  space group from 11.16 Å to 19.5 Å.<sup>[7]</sup> The Na ions are found to occupy different configurations from the parent compound, while the water forms a structure that replicates the structure of ice to a good approximation. It is interesting to note that the parent material has the Na(2) position at  $(2/3, 1/3, 1/4)$ , while the neutron patterns reveal that the intercalation of the water shifts this to  $(1/3, 2/3, 1/4)$  relative to the  $\text{CoO}_2$  layer, as shown in Fig. 2 - 11.<sup>[24]</sup> Moreover,  $\text{Na}_x\text{CoO}_2 \cdot y\text{H}_2\text{O}$  is a

layered system where the  $\text{Co}^{4+}$  ions are in the low-spin state and carry  $S = 1/2$  so that quantum effects are maximal, while the underlying  $\text{CoO}_2$  lattice is triangular rather than  $\text{CuO}_2$  square like the high- $T_c$  cuprates.<sup>[29]</sup> These observations suggest that this may be the new class of high- $T_c$  superconductors since the discovery of the cuprates over 20 years ago. The appropriate underlying model may be a Mott insulator in two-dimensions, with  $S = 1/2$  ( $t_{2g}^5$  for  $\text{Co}^{4+}$  in low spin state and  $t_{2g}^6 e_g^3$  for  $\text{Cu}^{2+}$ ),<sup>[29]</sup> where quantum fluctuations are optimal. The Co spins would then play a critical role in forming Cooper pairs that might have triplet symmetry as in  $\text{Sr}_2\text{RuO}_4$  or  $d$ -wave symmetry as in the cuprates. On the other hand, the traditional electron-phonon interaction may be establishing conventional  $s$ -wave pairing, with the possibility that the anharmonic motion of the hydrogen and oxygen ions might be playing a role in enhancing the superconducting properties, in a manner similar to  $\text{MgB}_2$ .<sup>[18]</sup>

### 2-1-3 Physical characteristics of $\text{Na}_x\text{CoO}_2$

Fig. 2 - 12(a) displays the systematic variation of the magnetic susceptibility  $\chi$  with Na content  $x$ .<sup>[31]</sup> At  $x = 0.75$ ,  $\chi$  is slightly rounded below 20 K, consistent with the appearance of a weak magnetization  $M$  ( $\sim 0.03 \mu_B$  per Co, with  $\mu_B$  the Bohr magneton), while a spin-density-wave (SDW) state at 0.75 had also been suggested.<sup>[8,12]</sup> According to those reported by Y. Wang *et al.*<sup>[31]</sup> and R. Ray *et al.*<sup>[32]</sup> for  $x \sim 0.68$ , although the resistivity is metallic, the magnetic susceptibility  $\chi$  displays a surprising Curie-Weiss profile that  $\chi = \chi_0 + C / (T - \theta)$ , with  $\theta \sim -70$  K, a negative Weiss temperature  $\theta$ , instead of the Pauli paramagnetic susceptibility.

With decreasing  $x$  below 0.68, the Curie-Weiss divergence in  $\chi$  is progressively

reduced with lowering  $x$  until it vanishes at  $x = 0.5$ . For  $\chi$  at 0.5 reveals the existence of two sharp cusps at  $T_{c1} = 88$  K and  $T_{c2} = 53$  K (arrows). These two transitions signal the onset of an insulating state.<sup>[31]</sup> In this charge-ordered state,  $\chi$  remains independent of the magnetic field  $H$ , which is inconsistent with magnetic ordering. As  $x$  lowers to 0.31, the profile of  $\chi$  becomes relatively featureless, although its magnitude remains large compared with the Pauli susceptibility in conventional metals.

Fig. 2 - 12(b) shows the in-plane resistivity  $\rho$  versus Na content  $x$ . At all  $x$  values except for  $x = 0.5$ ,  $\rho$  reveals metallic behavior. For example, the well-studied Curie-Weiss state ( $x = 0.68$  and  $0.71$ ), has a characteristic  $T$ -linear profile below 100 K.<sup>[5]</sup> At higher doping,  $x = 0.75$ , it shows a distinct change in slope near 20 K, reflecting the onset of the weak magnetic order. In contrast to these metallic states, insulating behavior abruptly appears at  $x = 0.5$ . Below  $T_{c2}$ , however,  $\rho$  rises rapidly to reach  $\sim 20$  m $\Omega$  cm at 4 K. This insulating state is confined to a narrow interval in  $x$  as shown in Fig. 1 - 1. At the lowest doping in the figure,  $x = 0.31$ , a metallic state has higher conductivity as compared with  $x = 0.71$  appears again. Moreover, the resistivity is highly anisotropic between in- and out-of-plane directions, and the in-plane resistivity is as low as 200 mV cm at 300 K, as shown in Fig. 2 - 13.<sup>[1]</sup>

Furthermore, in a neutral reference CoO<sub>2</sub> layer the nominal valence of the Co atom is Co<sup>4+</sup>, i.e., a  $3d^5$  ion. In a CoO<sub>6</sub> octahedral environment the  $3d$  levels are split as shown in Fig. 2 - 14.<sup>[13,31]</sup> The trigonal distortion of the oxygen octahedra causes further splitting of the  $3d$  levels. The lower threefold degenerate  $t_{2g}$  levels are split into a nondegenerate  $d_{z^2}$  state with a doublet below, denoted as  $e_g$  ( $t_{2g}$ ) in this figure. The ground state configuration is an orbital nondegenerate spin -1/2, low spin state. In this system, we choose the direction of trigonal distortion to be the  $z$ -axis, so the

top nondegenerate split orbital of the  $t_{2g}$  manifold is a  $3d_{z^2}$  orbital. Thus in the nominal charge state  $\text{Co}^{4+}$ , we have an unpaired electron in the  $d_{z^2}$  orbital, making  $\text{Co}^{4+}$  ground state an orbital nondegenerate spin -1/2 state. In the same way for  $\text{Co}^{3+}$  we have two electrons filling the  $d_{z^2}$  level making the ground state an orbital nondegenerate spin singlet. It is interesting to note that the  $\text{CoO}_2$  layer with strong trigonal distortion has escaped some important effects which should work against superconductivity, namely, Jahn-Teller distortion, Hund coupling, and possible high spin ground states of Co ions.<sup>[13]</sup>

Furthermore, a detailed band structure calculation for  $x = 0.5$  compound has been performed by Singh.<sup>[32]</sup> By using the local density approximation (LDA), it was found that the O  $2p$  bands are located well below the Fermi level and there is little hybridization between O  $2p$  and Co  $3d$  bands, as shown in Fig. 2 - 15.<sup>[33]</sup> The splitting between the Co  $3d e_g$  and  $t_{2g}$  bands is very large. The conduction electrons are mainly from the  $t_{2g}$  band and the  $e_g$  band is about 2.5 eV above the Fermi level. In the rhombohedral crystal field, the  $t_{2g}$  manifold is further split into two  $a_{1g}$  and four  $e'_g$  bands. The  $a_{1g}$  bands contribute a large cylindrical hole with Fermi surface centered at  $\Gamma$ . This large Fermi surface was confirmed by the angle-resolved photoemission spectroscopy (ARPES) measurements.<sup>[34-37]</sup>

The neutron experiments<sup>[38-40]</sup> indicate that the spin structure in  $\text{Na}_{0.75}\text{CoO}_2$  is three dimensional, with ferromagnetic fluctuation within the cobalt layers and antiferromagnetic fluctuation perpendicular to the layers. Metamagnetic transition observed in  $\text{Na}_{0.85}\text{CoO}_2$  is consistent with this feature,<sup>[41]</sup> revealing a clear anisotropy phenomenon for  $\text{Na}_x\text{CoO}_2$ .

Moreover, the specific heat measurement of  $\text{Na}_{0.68}\text{CoO}_2$  was reported by L. B. Luo *et al.*<sup>[42]</sup> who fitted the temperature-dependent specific heat ( $C - T$  diagram) by

$C = \gamma T + \beta T^3$  with  $\gamma = 34 \text{ mJ/mol K}^2$  and  $\beta = 0.06 \text{ mJ/mol K}^4$  (the Debye temperature  $\Theta_D = 492 \text{ K}$ ), where  $\gamma T$  and  $\beta T^3$  represent the contribution from electron and phonon, respectively. The large value of  $\gamma$  confirms the strong electron-electron correlation in the  $\text{Na}_x\text{CoO}_2$  systems.<sup>[43]</sup>

## 2-1-4 Thermoelectric properties of $\text{Na}_x\text{CoO}_2$

Determine whether one material has good thermoelectric transfer characteristics, done the standard by the level of dimensionless figure of merit  $ZT$ , defined as:<sup>[44]</sup>

$$ZT = S^2 T / \rho \kappa , \quad (2.1.1)$$

where  $S$  is the Seebeck coefficient (or thermopower which is defined by  $E / |\nabla T|$ , where  $E$  is the electric field and  $\nabla T$  is the gradient of temperature),  $\rho$  is the resistivity, and  $\kappa$  is the thermal conductivity. Among this equation, we know that there should be the following characteristics for a good thermoelectric material:

1. Large Seebeck coefficient  $S$ , make the material have better ability to let heat energy and electric energy change each other.
2. Low resistivity  $\rho$ , reduce the power losses due to the generated heat of resistance.
3. Low thermal conductivity  $\kappa$ , be apt to maintain the temperature difference of both ends of sample.

But above-mentioned three pieces of properties will influence each other, usually the electric conductivity of the conventional metal is fine, but the

thermopower is extremely small because of the flow of electrons induced by  $-\nabla T$  is nearly cancelled by a parallel flow of electric holes.

The high thermopower and low resistivity of  $\text{NaCo}_2\text{O}_4$  were first found in 1997 by I. Terasaki *et al.*<sup>[1]</sup> with its  $ZT_{300\text{K}} \sim 1$ , was the largest record up to now. It is important to note that  $\text{NaCo}_2\text{O}_4$  has low mobility ( $13 \text{ cm}^2/\text{Vs}$  at 300 K), which is strikingly against the common sense that a low-mobility conductor cannot be a thermoelectric material. Scientists had tried to find out the reason why such high thermopower exists in  $\text{Na}_x\text{CoO}_2$  by nuclear spin-resonance experiments,<sup>[28]</sup> heat capacity,<sup>[43]</sup> and Hall effect,<sup>[45]</sup> but it remained an enigma until 2003, at that time Y. Wang *et al.* performed measurements in applied magnetic fields and indicated that spin entropy dominates the enhancement of thermopower in  $\text{Na}_x\text{CoO}_2$ .<sup>[3]</sup> Moreover, because the spin-entropy current is in the direction of the charge current, this contribution to thermopower  $S$  is positive (hole-like) as observed. The elementary charge-transport process is the hopping of a hole from  $\text{Co}^{4+}$  to  $\text{Co}^{3+}$  (Fig. 2 - 14(b)).

In 2006, M. Lee *et al.* reported that, for high-doping region  $x > 0.75$ ,  $S$  undergoes a large enhancement, as shown in Fig. 2 - 16.<sup>[45,46]</sup> At the critical doping  $x_p \sim 0.85$ ,  $Z$  (at 80 K) reaches values  $\sim 1.8 \times 10^{-3} \text{ K}^{-1}$  is among the highest known for a hole-type material below 100 K, revealing a good expectation for application in low-temperature thermoelectric material.

## 2-2 Review of previous optical work

### 2-2-1 Raman scattering

Raman-scattering measurement is an efficient way for understanding the structural and electronic properties of solids. By analyzing the numbers and frequencies of Raman phonon modes, we can gain lots of information such as compositional and symmetry phenomena from various conditions of  $\text{Na}_x\text{CoO}_2$ . Recently, there are several interesting results in the Raman-scattering characterization of  $\text{Na}_x\text{CoO}_2$  system.<sup>[23,47-53]</sup> However, these reported Raman-scattering spectra of  $\text{Na}_x\text{CoO}_2$  show contradictory. In order to explicate it, we use the Raman spectra reported by H. X. Yang *et al.*<sup>[52]</sup> showing in Fig. 2 - 17 as an example. In this figure, there are two Raman active phonons for  $\alpha$ - $\text{NaCoO}_2$ , three Raman active phonons for  $\beta$ - $\text{Na}_{0.6}\text{CoO}_2$ , and five Raman peaks for  $\gamma$ - $\text{Na}_{0.75}\text{CoO}_2$ .

For  $\alpha$ - $\text{NaCoO}_2$  polycrystal with hexagonal structure and  $R-3m$  space group, there are two Raman active phonons, similar to those reported by M. N. Iliev *et al.* for  $x = 0.7$  single crystal,<sup>[23]</sup> J. F. Qu *et al.* for  $x = 0.3$  and  $0.7$  single crystals,<sup>[51]</sup> and P. Lemmens *et al.* for  $x = 0.83, \sim 1$ ,<sup>[49]</sup> and  $\text{Na}_{0.35}\text{CoO}_2 \cdot 1.3\text{H}_2\text{O}$  single crystals<sup>[48]</sup> with hexagonal crystal structure and  $P6_3/mmc$  space group for these three teams above, revealing these spectra are indistinguishable even for various Na concentrations, two different space groups ( $R-3m$  and  $P6_3/mmc$ ), and hydrated type.

For  $\gamma$ - $\text{Na}_{0.75}\text{CoO}_2$  polycrystal with hexagonal structure and  $P6_3/mmc$  space group, there are five Raman active phonons, similar to those reported by K. Takada *et al.* for  $\text{Na}_{0.35}\text{CoO}_2 \cdot 1.3\text{H}_2\text{O}$  powder<sup>[53]</sup> and Y. G. Shi *et al.* for  $x = 0.75$  NaCl-flux grown single crystal with hexagonal crystal structure and  $P6_3/mmc$  space group.<sup>[47]</sup> In contrary, J. F. Qu *et al.*<sup>[51]</sup> suggested that this spectrum containing five Raman

phonon modes should belong to  $\text{Co}_3\text{O}_4$  rather than  $\text{Na}_x\text{CoO}_2$ . Very recently, P. Lemmens *et al.* reported that the Raman data of NaCl-flux grown  $\text{Na}_x\text{CoO}_2$  are most probably interfered by a degradation of the sample leading to a surface layer of  $\text{Co}_3\text{O}_4$ .<sup>[54]</sup> Such impurity will influence on the application of thermoelectric materials. In our research, we give not only a clear Raman phonon assignment of the interesting  $\text{Na}_x\text{CoO}_2$  systems, but also a reasonable elaboration for the incompatible observations of Raman-scattering spectra in Chapter 5.

## 2-2-2 Infrared measurements

The infrared spectroscopy yields important information about electronic structure and charge dynamics of the system. The far-infrared conductivity spectra of  $\text{Na}_x\text{CoO}_2$  ( $x = 0.50, 0.57, 0.75, 0.85, 0.95,$  and 1) single crystals reported by S. Lupi *et al.*<sup>[55]</sup> were shown in Fig. 2 - 18. Obviously, a phonon mode at around  $590 \text{ cm}^{-1}$  is observed in all six spectra which is assigned to  $E_{1u}$  in-plane vibration. At low frequencies, the  $x = 0.57$  sample exhibiting a clear metal-like behavior with a Drude band appears at zero frequency, while the  $x = 0.5$  sample shows insulating behavior, consistent with the resistivity measurement shown in Fig. 2 - 12(b). A far-infrared peak at about  $150 \text{ cm}^{-1}$  in  $\sigma_1(\omega)$ , which coexists with a small Drude contribution, indicates charge localization in the  $\text{CoO}_2$  layers. Moreover, for  $x = 0.75, 0.85,$  and  $0.95$  samples a far-infrared peak at about  $100 \text{ cm}^{-1}$  hardens dramatically below 30 K, pointing towards a strong coupling of the charge and spin degrees of freedom. In contrast with these results, the  $x = 0.57$  sample shows a metallic conduction at each temperature, described by an “anomalous Drude” behavior in the far-infrared  $\sigma_1(\omega)$ . Such behavior has also been found in  $\text{Na}_x\text{CoO}_2$

systems with  $x = 0.18, 0.32, 0.36, 0.7, 0.82,$  and  $0.85$  single crystals,<sup>[37,56-59]</sup> revealing this phenomenon seems to be independent with Na concentration. Therefore, because of such behavior, the metallic component of  $\sigma_1(\omega)$  cannot be fully reproduced by a simple Drude term which is the most common description for simple metals, also successfully applied in several oxides. The effective metallic component of the optical conductivity can be alternatively described in terms of an "anomalous-Drude" model,<sup>[56]</sup> where both the effective mass  $m^*(\omega)/m_b$  and the scattering rate  $1/\tau(\omega)$  of the itinerant charge carriers are allowed to depend on frequency. S. Lupi *et al.*<sup>[56]</sup> measured the optical conductivity of  $\text{Na}_{0.57}\text{CoO}_2$  single crystal and reported that the charge carrier has an effective mass of  $5m_b$  and the scattering rate is  $1/\tau(\omega) \sim \omega^{3/2}$ , while G. Caimi *et al.*<sup>[60]</sup> reported that for  $\text{Na}_{0.7}\text{CoO}_2$  single crystal the effective mass is the same as the former but the scattering rate is  $1/\tau(\omega) \sim \omega$ , indicative of a non-Fermi liquid behavior in  $\text{Na}_{0.7}\text{CoO}_2$ .

Table. 2 - 1. The types of structures found for the  $\text{Na}_x\text{CoO}_2$  compounds ( $0.3 < x < 1$ ). The structure types are (distinguished by Na coordination type and the number of layers per unit cell) *P2*, prismatic, two layers; *O3*, octahedral, three layers; *P1*, prismatic, one layer; *O1*, octahedral, one layer. Where a, b, c, and d are data from reference 16, 17, 13, and 18 respectively.<sup>[13]</sup>

Refined composition	Space group	Sodium coordination	Structure type
Two-layer structures			
$\text{Na}_{0.34}\text{CoO}_2^{\text{a}}$	$P6_3/mmc$	Trigonal prism	<i>P2</i>
$\text{Na}_{0.5}\text{CoO}_2^{\text{b}}$	$Pnmm$	Trigonal prism	<i>P2</i>
$\text{Na}_{0.63}\text{CoO}_2^{\text{a}}$	$P6_3/mmc$	Trigonal prism	<i>P2</i>
$\text{Na}_{0.71}\text{CoO}_2^{\text{a}}$	$P6_3/mmc$	Trigonal prism	<i>P2</i>
$\text{Na}_{0.76}\text{CoO}_2^{\text{a}}$	$P6_3/mmc$	Trigonal prism	<i>P2</i>
$\text{Na}_{0.80}\text{CoO}_2^{\text{a}}$	$P6_3/mmc$	Trigonal prism	<i>P2</i>
$\text{Na}_1\text{CoO}_2^{\text{a}}$	$P6_3/mmc$	Trigonal prism	<i>P2</i>
Three-layer derived structures			
$\text{Na}_{0.32}\text{CoO}_2^{\text{c}}$	$R\bar{3}m$	Octahedral	<i>O3</i>
$\text{Na}_{0.5}\text{CoO}_2^{\text{c}}$	$C2/m$	Trigonal prism	<i>P1</i>
$\text{Na}_{0.6}\text{CoO}_2^{\text{c}}$	$C2/m$	Trigonal prism	<i>P1</i>
$\text{Na}_{0.67}\text{CoO}_2^{\text{d}}$	$C2/m$	Trigonal prism	<i>P1</i>
$\text{Na}_{0.75}\text{CoO}_2^{\text{c}}$	$C2/m$	Octahedral	<i>O1</i>
$\text{Na}_{0.92}\text{CoO}_2^{\text{c}}$	$R\bar{3}m$	Octahedral	<i>O3</i>

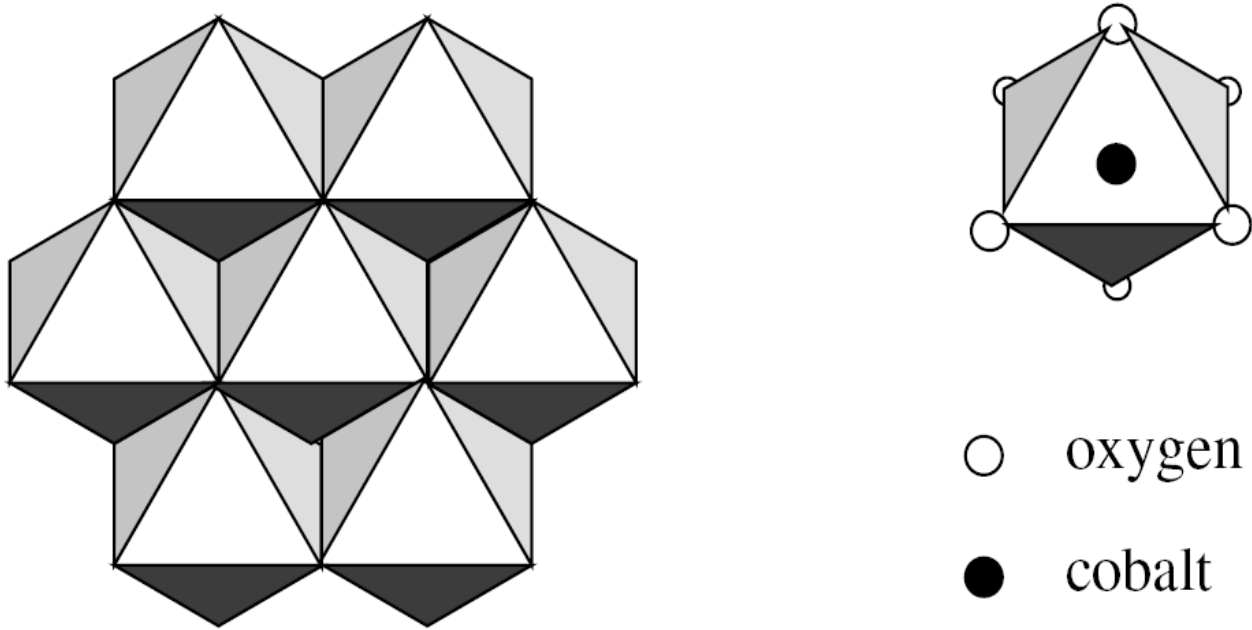


Fig. 2 - 1. Structure of  $\text{CoO}_2$  layer. A triangular network of edge sharing oxygen octahedra. Co atoms are at the center of the oxygen octahedra.<sup>[13]</sup>

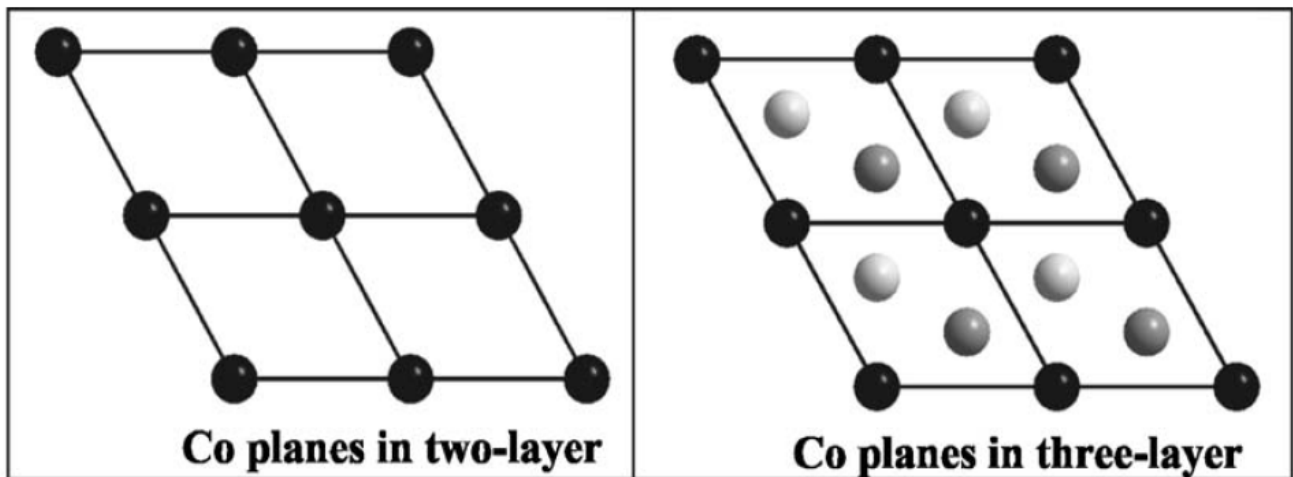


Fig. 2 - 2. A comparison of the Co positions in the two-layer and three-layer variants. In the two-layer phases the Co planes are the same in all layers. In the three-layer derived phases the triangular Co planes are staggered: black balls represent layer 1, dark gray balls represent layer 2, and light gray balls represent layer 3.<sup>[14]</sup>

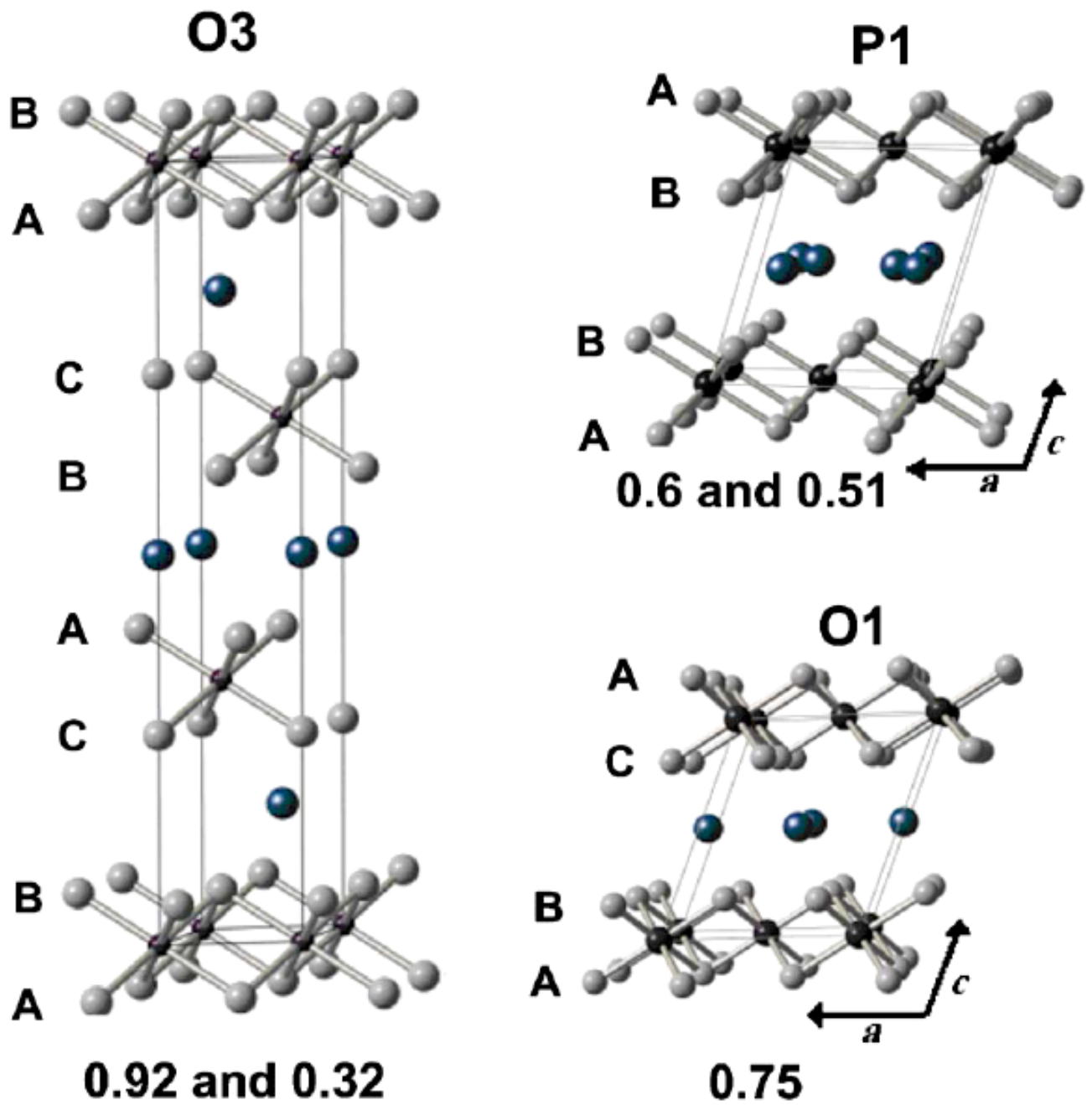


Fig. 2 - 3. The crystal structures of  $\text{Na}_x\text{CoO}_2$  phases ( $x = 0.92, 0.75, 0.6, 0.51,$  and  $0.32$ ) derived from three-layer  $\text{NaCoO}_2$ . Smaller and bigger black spheres represent Co and sodium ions, respectively, while the gray spheres are the oxygen ions.<sup>[14]</sup>

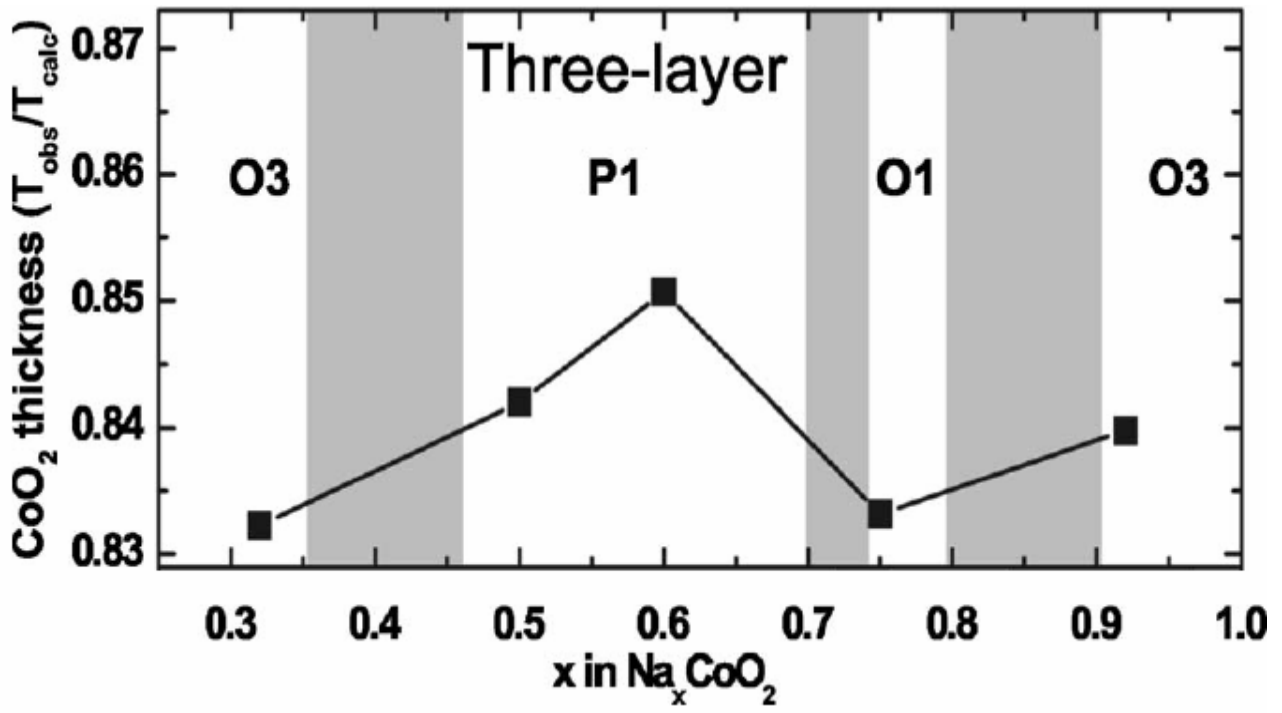


Fig. 2 - 4. The thickness of the CoO<sub>2</sub> plane relative to the thickness expected for an ideal CoO<sub>6</sub> octahedron (ideal thickness = 1) as a function of  $x$  in three-layer derived Na <sub>$x$</sub> CoO<sub>2</sub>.<sup>[14]</sup>

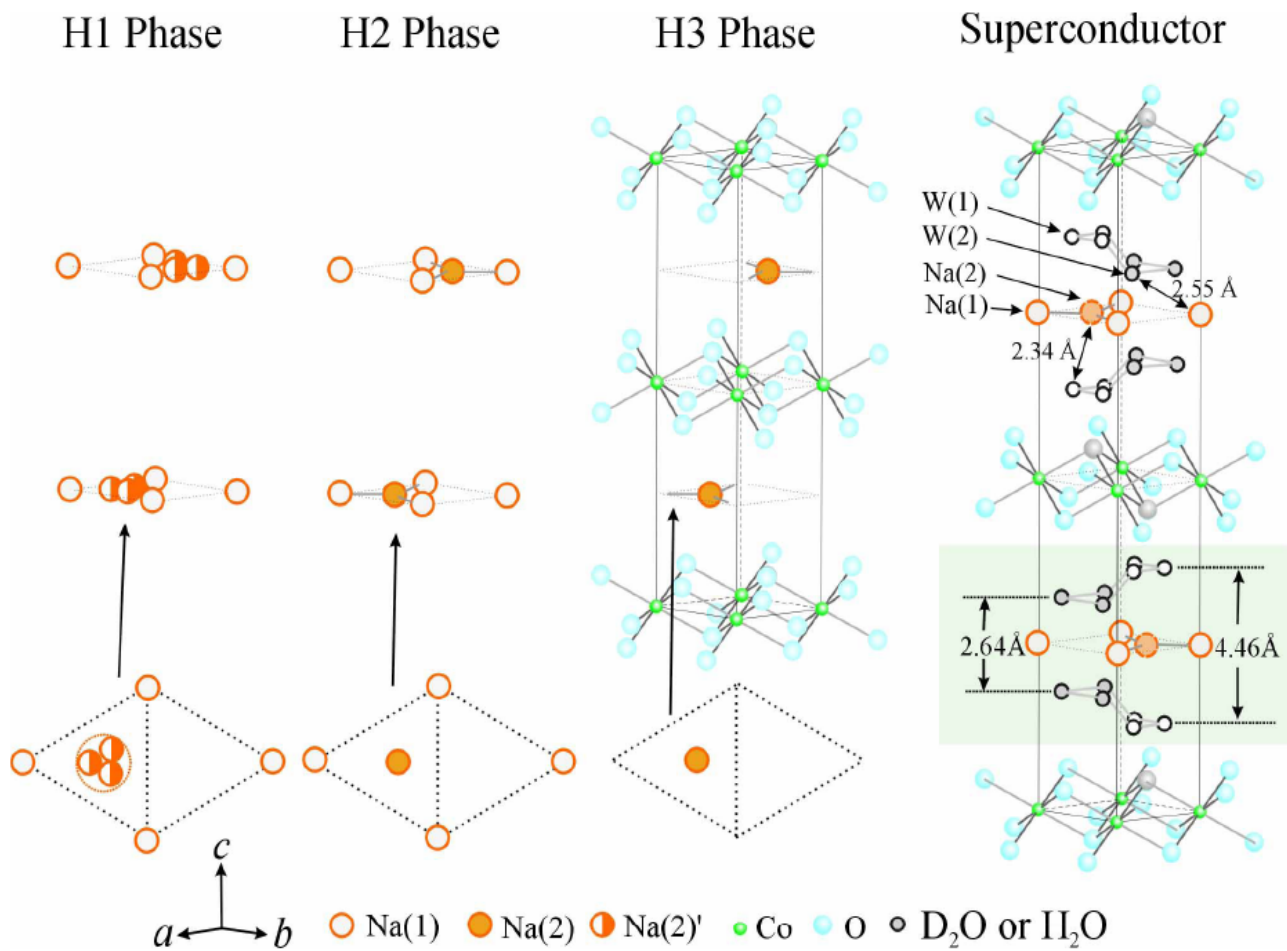


Fig. 2 - 5. Three different structures ( $H1$ ,  $H2$ , and  $H3$ ) that are controlled by the Na ions in  $\text{Na}_x\text{CoO}_2$ . At lower Na concentrations the Na(2) ions are randomly located at one of three positions that are symmetrically shifted off-center (designated Na(2)'), while at higher Na content the Na(2) occupancy is at the centered position. The structure on the right is for the superconductor, where we note that the Na ions shift to the other side of the unit cell to accommodate the ice-like layers of water.<sup>[7]</sup>

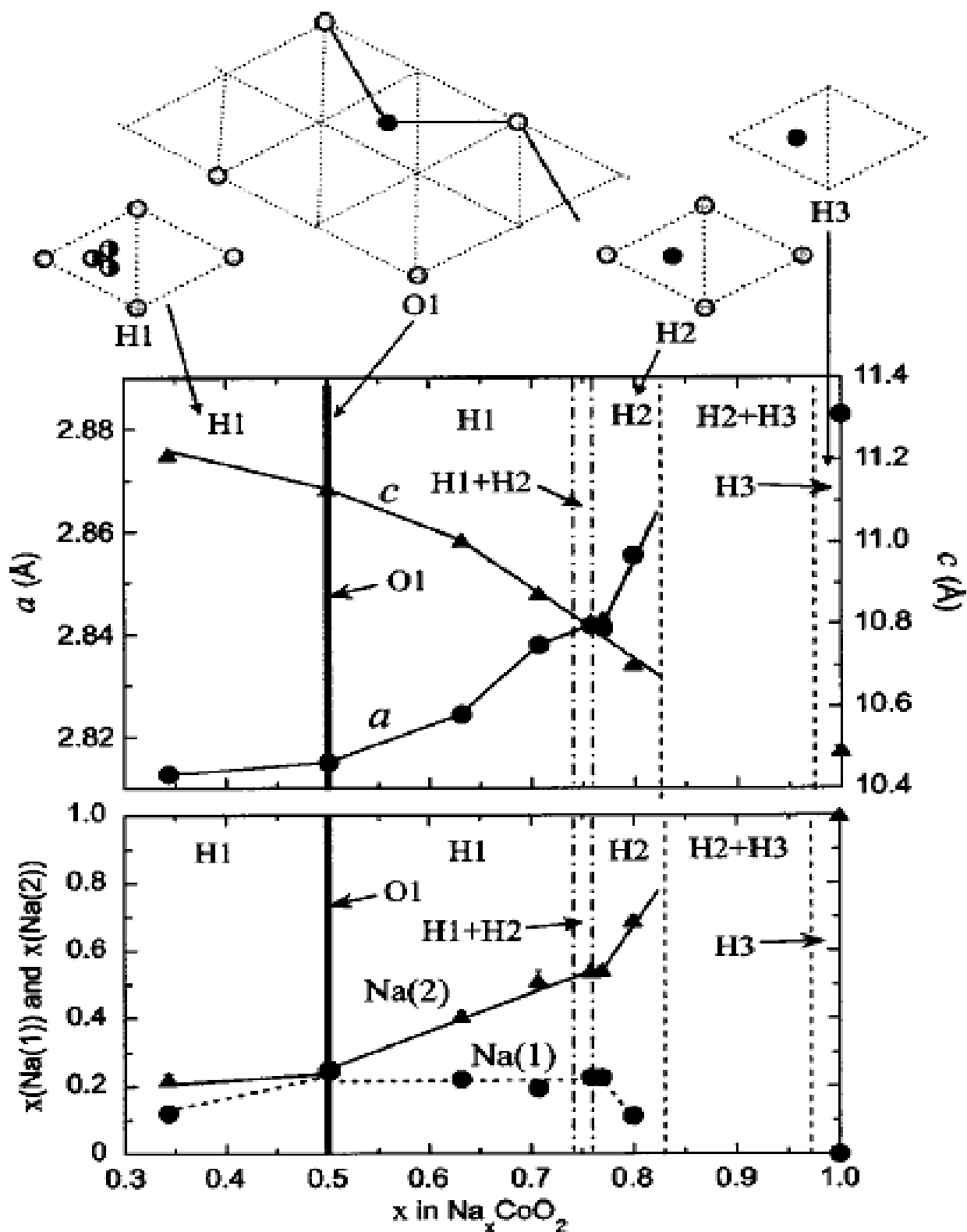


Fig. 2 - 6. The general structural characteristics and compositional stability regions of the four  $\text{Na}_x\text{CoO}_2$  phases. Upper panel, hexagonal crystallographic cell parameters. Lower panel, fractional occupancies of the two types of sodium sites:  $\text{Na}(1)$  shares faces with the  $\text{CoO}_6$  octahedra, and  $\text{Na}(2)'$  and  $\text{Na}(2)$  (plotted as one site) share edges with the  $\text{CoO}_6$  octahedra. Above the panels, the sodium ion distributions in the four phases are shown schematically.<sup>[19]</sup>

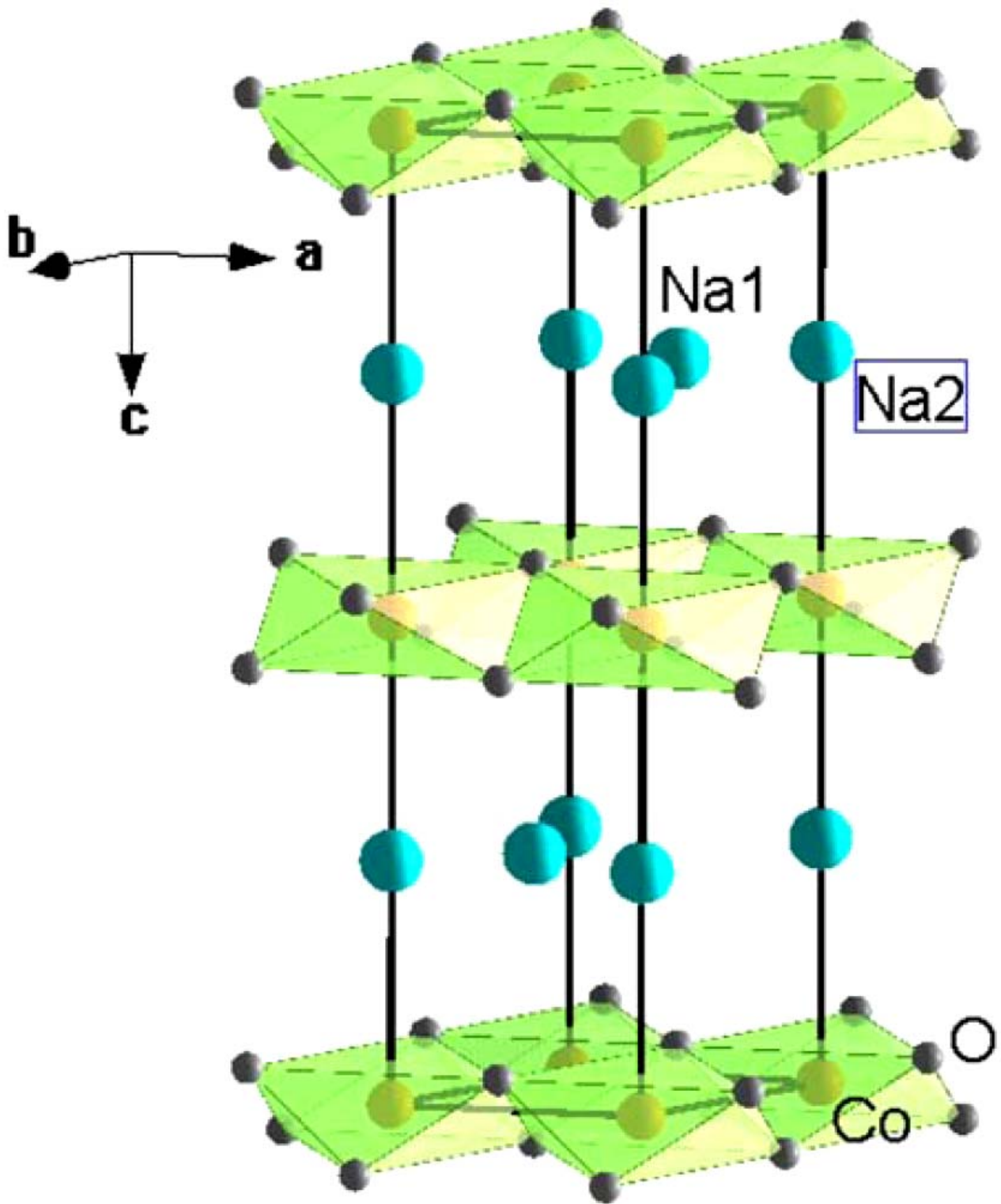


Fig. 2 - 7. Elementary cell of NaCoO<sub>2</sub>, showing the distorted CoO<sub>6</sub> octahedra.<sup>[23]</sup>

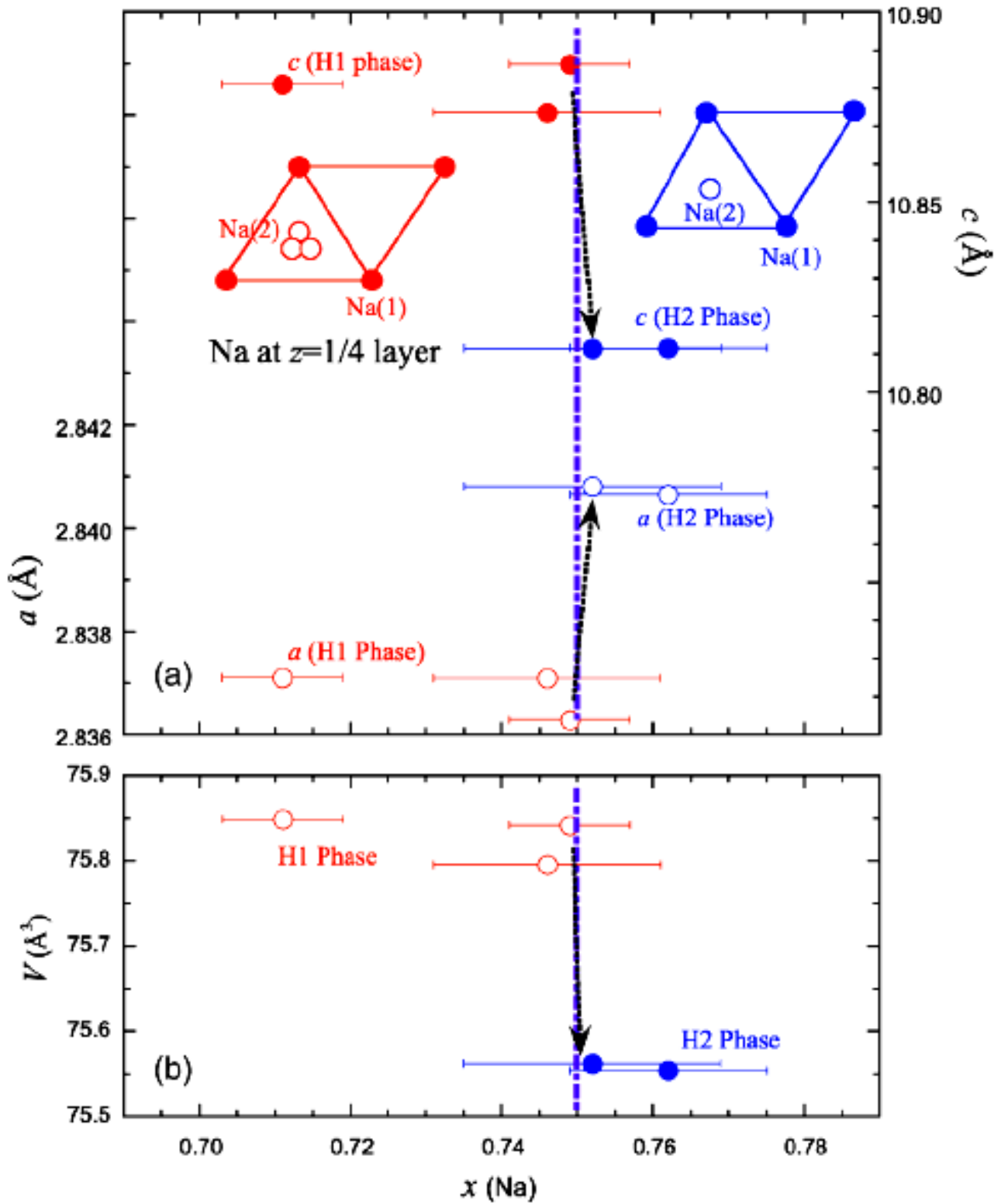


Fig. 2 - 8. Lattice parameters at room temperature as a function of Na content  $x$ . The change in the lattice constants as  $x$  increases above  $x \sim 0.75$  corresponds to the change from the  $H1$  structure to the  $H2$  structure.<sup>[25]</sup>

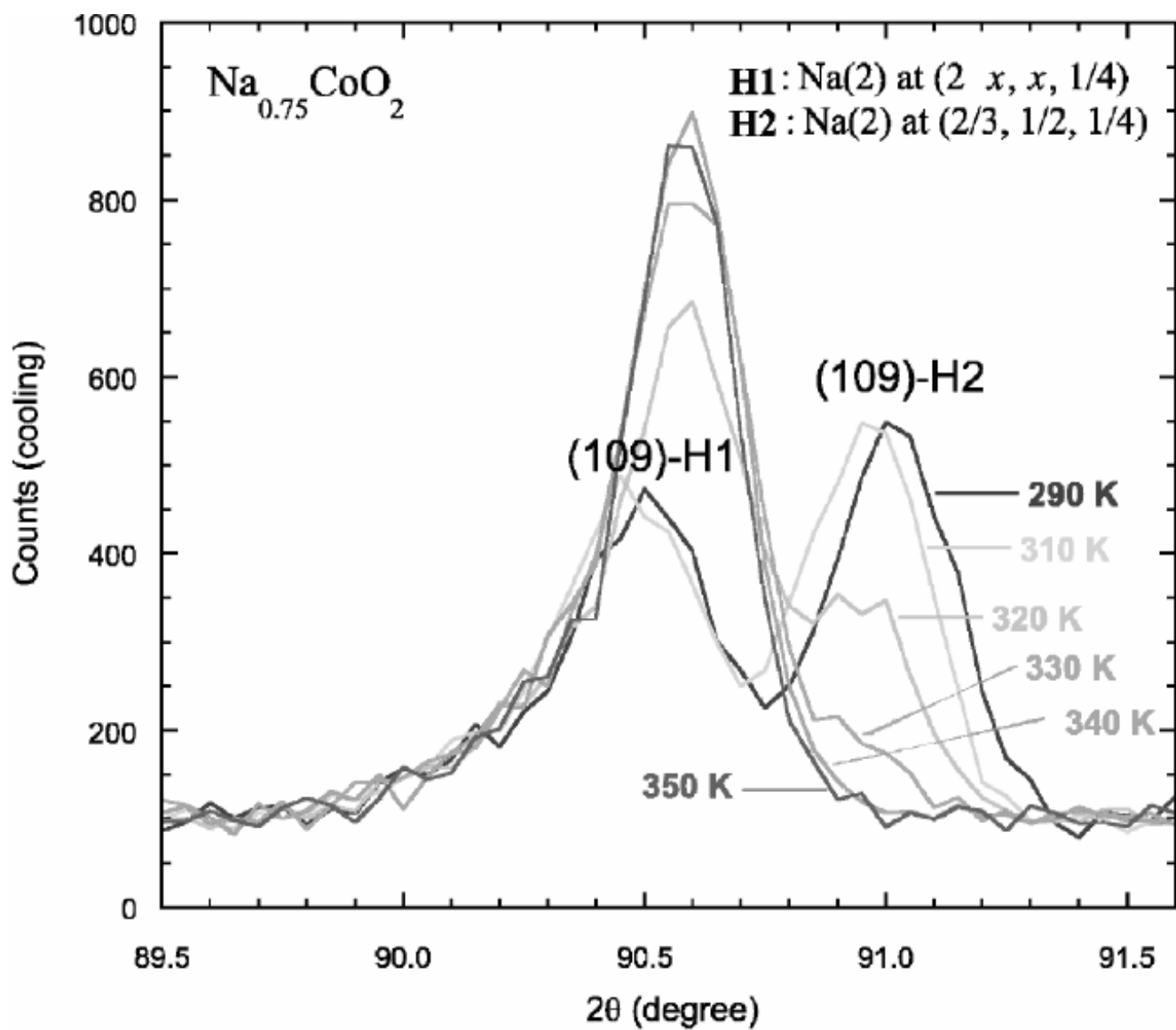


Fig. 2 - 9. Scans through the (109) Bragg peak of  $\text{Na}_{0.75}\text{CoO}_2$  powder sample at various temperatures.<sup>[25]</sup>

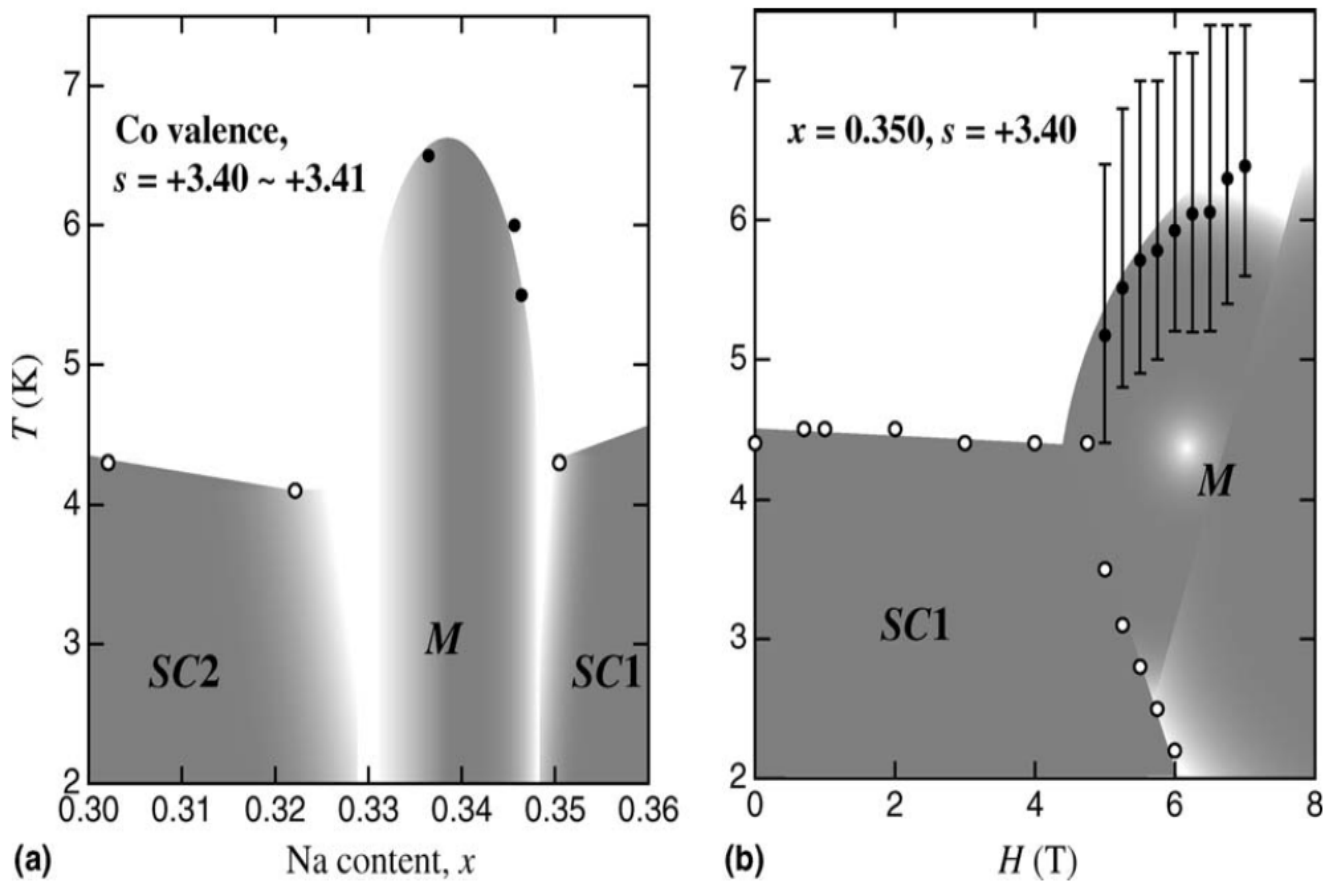


Fig. 2 - 10. (a) The  $x - T$  phase diagram and (b)  $H - T$  phase diagram. The open and closed circles represent  $T_c$  and the magnetic ordering temperature, respectively.<sup>[28]</sup>

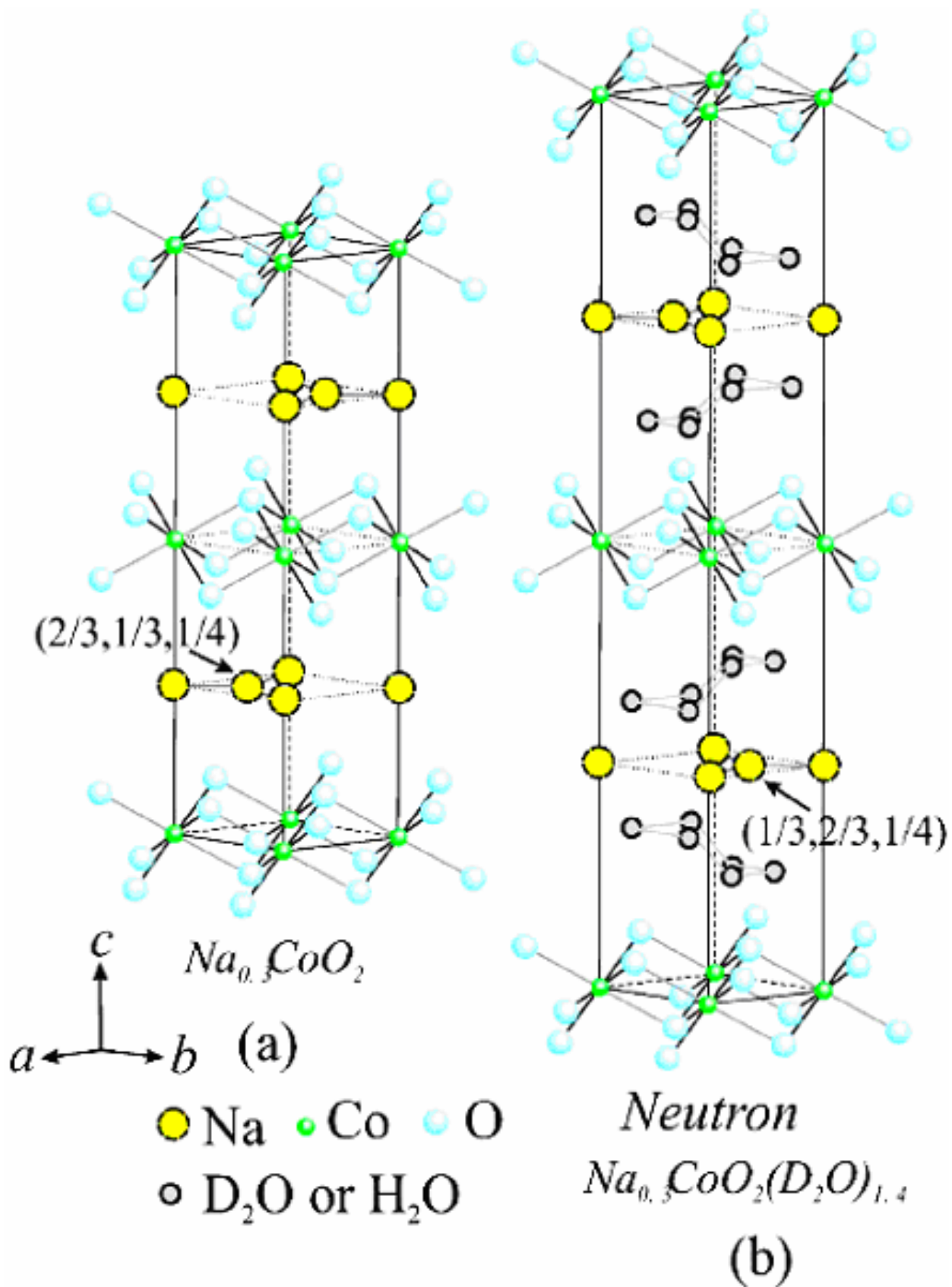


Fig. 2 - 11. Structures of (a)  $Na_{0.5}CoO_2$ , (b) the superconducting phase model.<sup>[24]</sup>

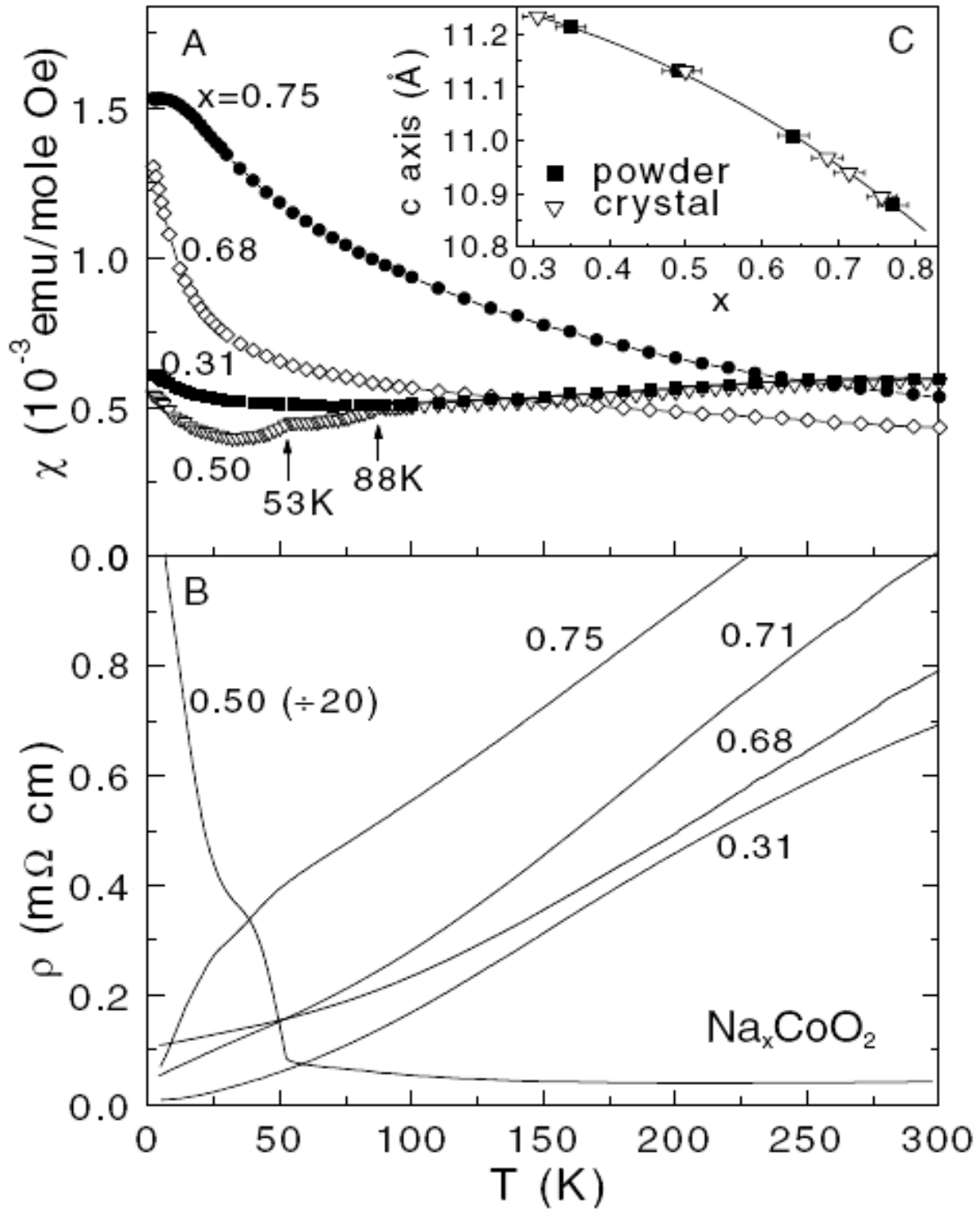


Fig. 2 - 12. (a) The susceptibility  $\chi$  and (b) in-plane resistivity  $\rho$  of single crystals of  $\text{Na}_x\text{CoO}_2$  with  $x$  determined by ICP. In panel (a),  $\chi$  is measured in an in-plane field  $H = 5\text{ T}$  ( $H \perp \hat{c}$ ). In the crystal with  $x = 0.75$ ,  $\chi$  fits the Curie-Weiss form  $\chi = C / (T + \theta)$ , with  $\theta \sim 150\text{ K}$  and  $C = 0.224\text{ emu K/Oe mole}$ . For  $x = 0.5$ , sharp transitions are observed at  $T_{C1}$  and  $T_{C2}$  (arrows). Panel (b) shows the  $T$  dependence of  $\rho$  at selected  $x$ . Insulating behavior is observed at  $x = 0.5$  (data displayed at lower scale), in contrast to metallic behavior in the rest. At low  $T$ ,  $\rho$  is  $T$  linear for  $x = 0.71$  but varies as  $T^2$  for  $x = 0.3$ . In panel (c), the  $c$ -axis lattice parameter measured by XRD is plotted against the Na content  $x$  fixed by ICP in powder samples.<sup>[31]</sup>

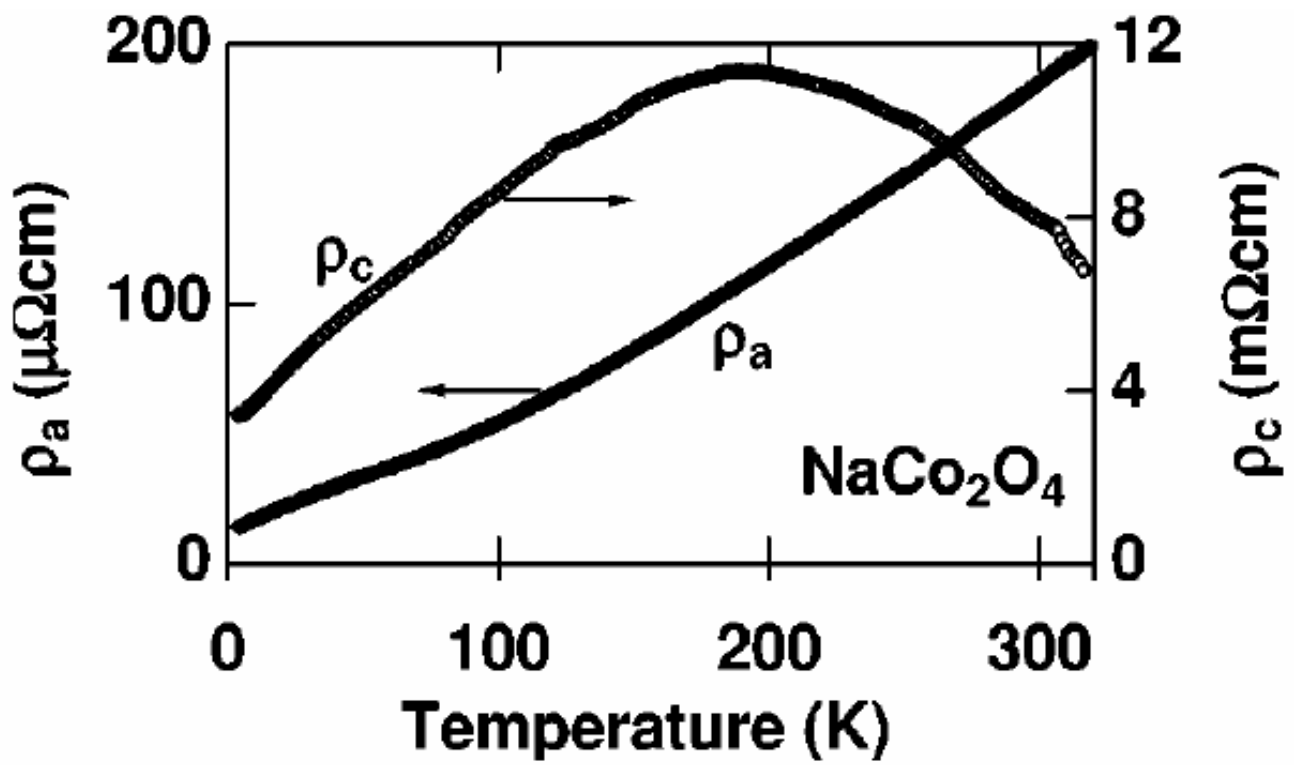


Fig. 2 - 13. In-plane ( $\rho_a$ ) and out-of-plane ( $\rho_c$ ) resistivity of  $\text{NaCo}_2\text{O}_4$  single crystals.<sup>[1]</sup>

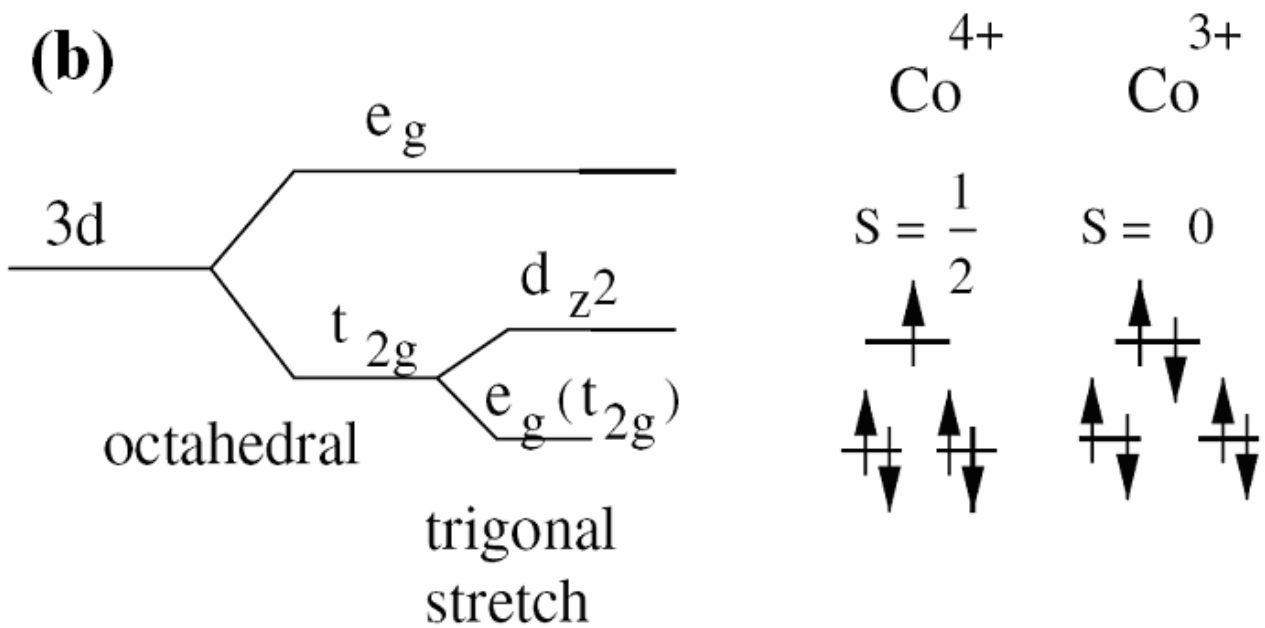
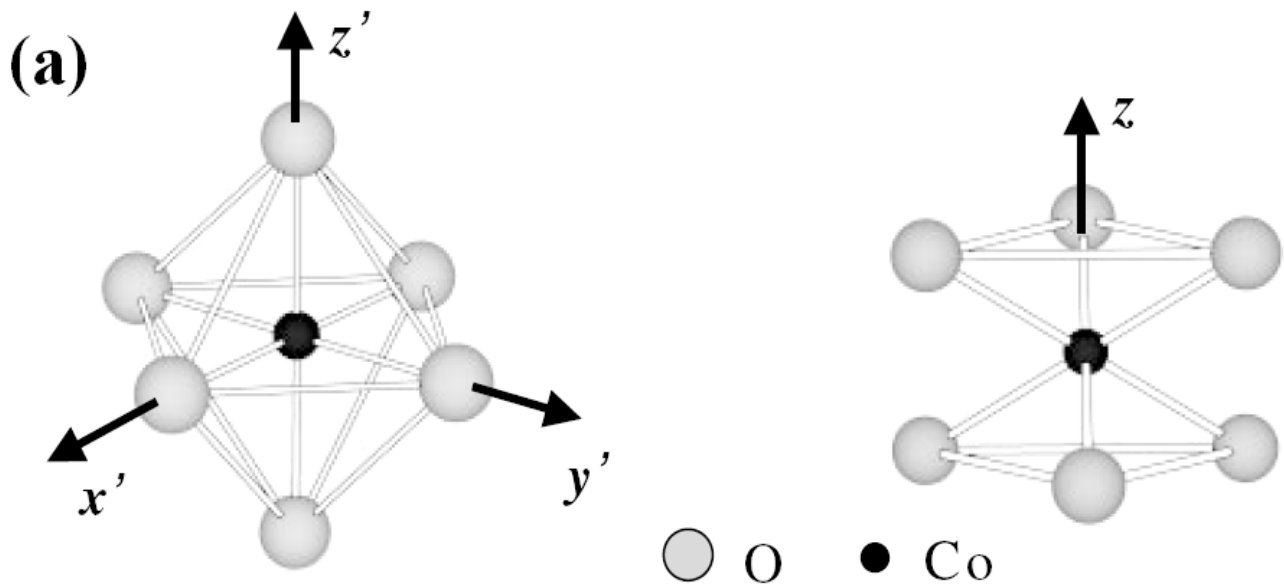


Fig. 2 - 14. (a) Illustration of the trigonal distortion of a CoO<sub>6</sub> octahedron. Left panel: undistorted CoO<sub>6</sub> octahedron with cubic ( $O_h$ ) symmetry. Right panel: compressed CoO<sub>6</sub> octahedron with  $D_{3d}$  symmetry. The distorted CoO<sub>6</sub> is rotated such that the threefold rotation axis is along the  $c$ -axis.<sup>[30]</sup>  
 (b) Crystal field split  $3d$  levels of cobalt.<sup>[13]</sup>

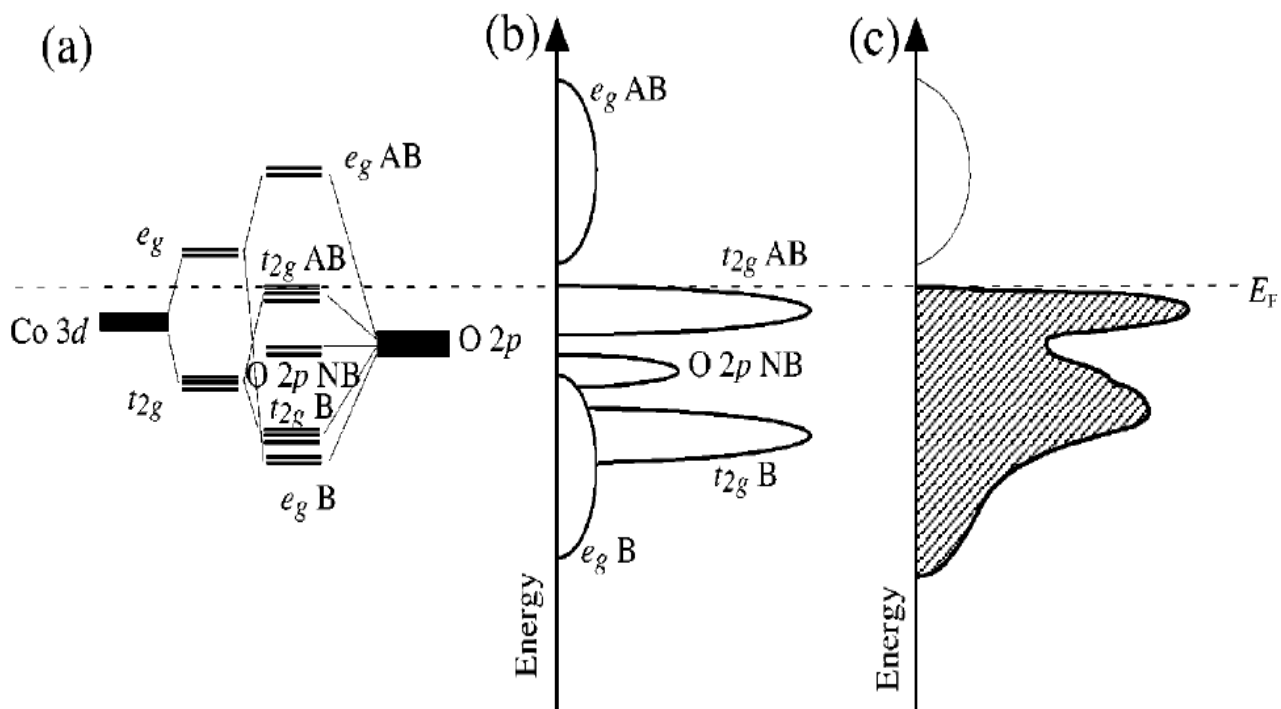


Fig. 2 - 15. Schematic illustration of (a) cluster levels in the CoO<sub>6</sub> octahedron, (b) the density of states in the network of the CoO<sub>6</sub> octahedrons, and (c) XPS spectrum expected to be observed for the network of the CoO<sub>6</sub> octahedrons.<sup>[33]</sup>

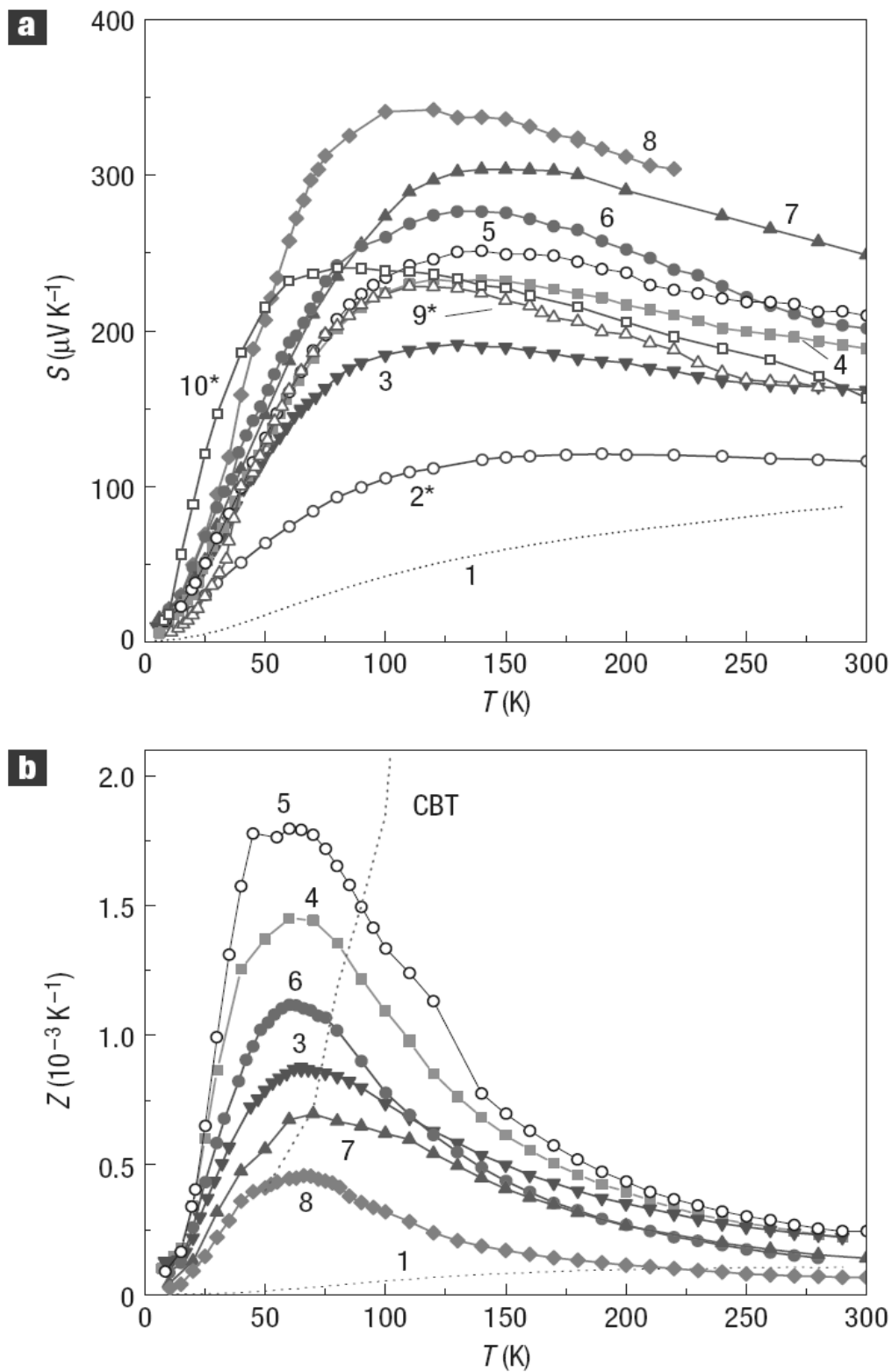


Fig. 2 - 16. (a) The in-plane thermopower  $S$  and (b) the figure of merit  $Z$  in  $\text{Na}_x\text{CoO}_2$ , where the samples are numbered in order of increasing  $x$ : sample 1 ( $x \sim 0.71$ ), 2 ( $x \sim 0.75$ ), 3 ( $x \sim 0.80$ ), 4 ( $x \sim 0.85$ ), 5 ( $x \sim 0.88$ ), 6 ( $x \sim 0.89$ ), 7 ( $x \sim 0.96$ ), 8 ( $x \sim 0.97$ ), 9 ( $x \sim 0.99$ ) and 10 ( $x \sim 1.0$ ). The dashed line labeled CBT is  $Z$  reported by C. Y. Chung *et al.* for  $\text{CsBi}_4\text{Te}_6$ .<sup>[45,46]</sup>

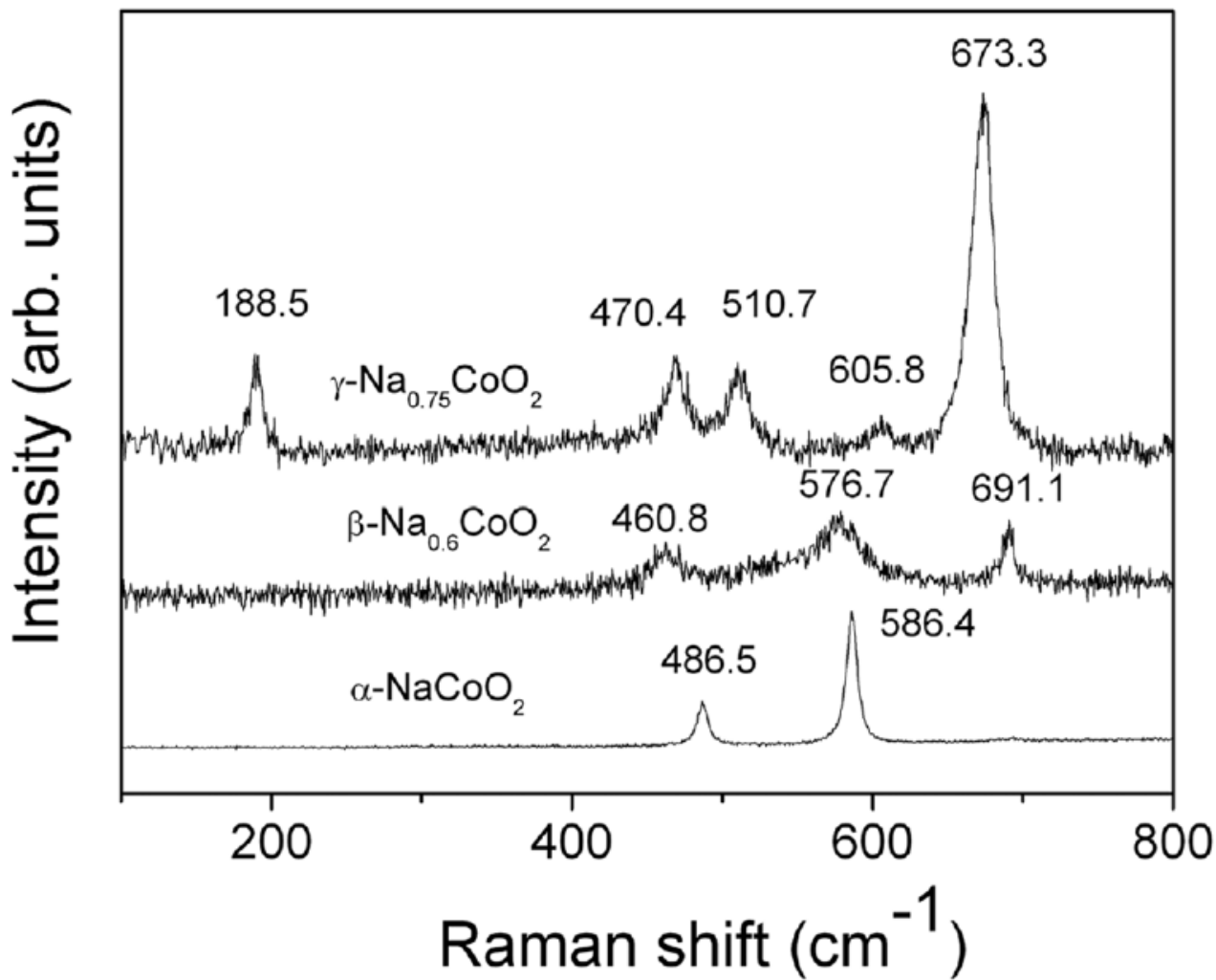


Fig. 2 - 17. Raman spectra of the  $\alpha\text{-NaCoO}_2$ ,  $\beta\text{-Na}_{0.6}\text{CoO}_2$ , and  $\gamma\text{-Na}_{0.75}\text{CoO}_2$  phases, demonstrating different spectral structures for these specific phases.<sup>[52]</sup>

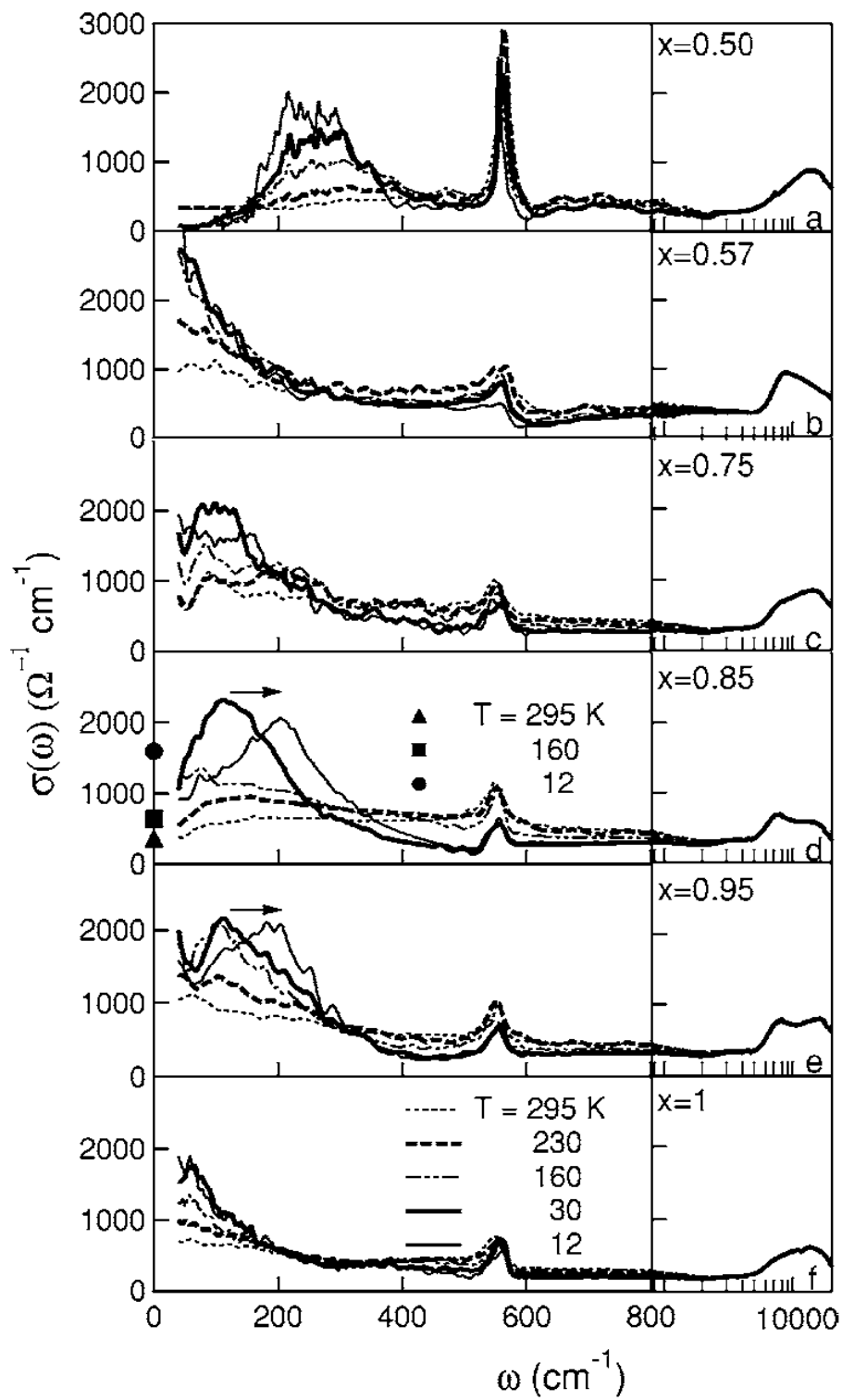


Fig. 2 - 18. Real part of the infrared conductivity of  $\text{Na}_x\text{CoO}_2$  for  $0.5 \leq x \leq 1$ , at different temperatures. For the sample with  $x = 0.57$ , the lowest two temperatures are 90 and 20 K. The arrows mark the strong displacement below 30 K of the far-infrared peak in both samples with high and incommensurate doping ( $x = 0.85$  and  $0.95$ ). For  $x = 0.85$ , dc conductivity values measured on the same sample are reported at three selected temperatures.<sup>[55]</sup>